Supplementary Information

Insight into the degradation mechanisms of Atomic Layer Deposited TiO_2 as photoanode protective layer.

Carles Ros[a,*], *Nina M. Carretero*[a], *Jeremy David*[c], *Jordi Arbiol*[c,d], *Teresa Andreu*[a,*], *Joan R. Morante*[a,b]

[a] Catalonia Institute for Energy Research (IREC). Jardins de les Dones de Negre 1, 08930 Sant Adrià del Besòs, Barcelona, Spain

[b] Universitat de Barcelona (UB), Martí i Franquès, 1, 08028 Barcelona, Spain

[c] Catalan Institute of Nanoscience and Nanotechnology (ICN2), CSIC and BIST, Campus UAB, Bellaterra, 08193 Barcelona, Spain

[d] ICREA, Pg. Lluís Companys 23, 08010 Barcelona, Spain

Corresponding authors: *cros@irec.cat, *tandreu@irec.cat

Figure S1. Picture of a p^+n-Si photoanode presenting the 1.2 x 1.2 cm^2 Si chip with an active area of 1 x 1 cm^2, defined by a perimeter of 100 nm of SiO_2 thick insulator layer. The Si chip was protected by TiO_2-ALD and Ag paint soldered to a Cu wire, and further encapsulated with epoxy resin.

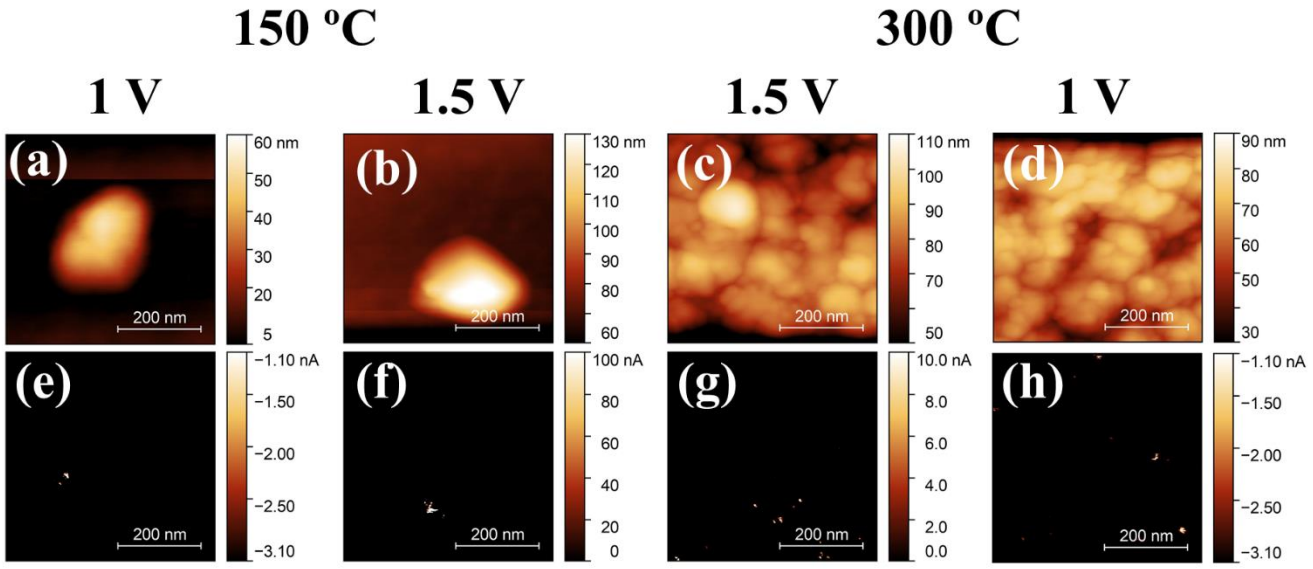

Figure S2. AFM height map of TiO_2 + NiFe layers grown at 150 ºC (a, b) and 300 ºC (c, d), and its respective current intensity maps, at potentials of 1 V (e, h) and 1.5 V (f, g).

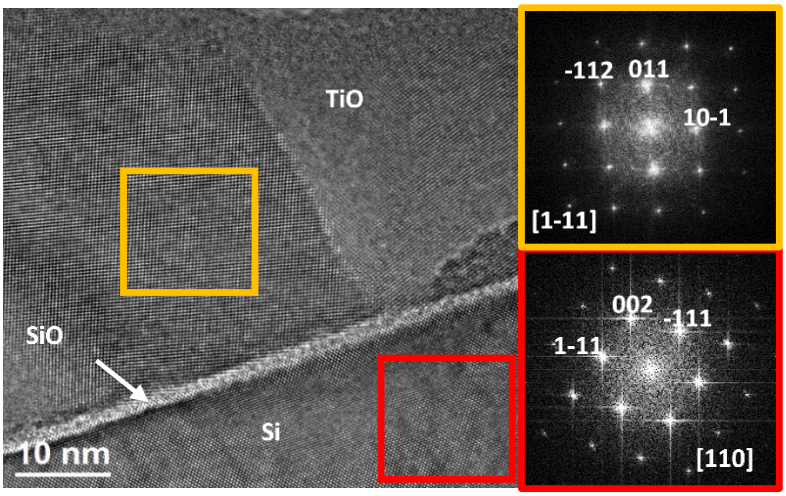

Figure S3. HRTEM image of the TiO_2-300 ºC interface with Si chip. Insets present the FFT of indicated regions: in yellow, anatase TiO2 crystal planes are observed; in red, the silicon monocrystalline substrate.

An intermediate 1.5-2 nm amorphous SiO_x native oxide layer can be seen between Si/TiO_2 interface. As Si photoanodes had been HF-etched immediately before ALD-TiO_2 deposition, the formation of this observed SiO_x is be attributed to the ALD process, when H_2O pulses first reach Si during synthesis.

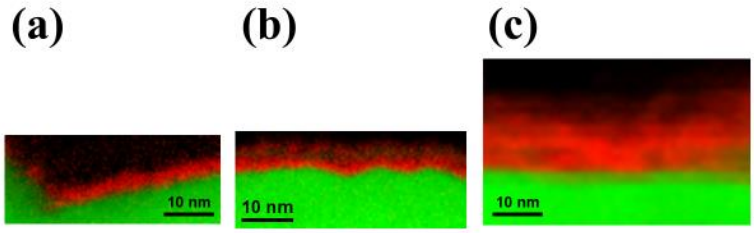

Figure S4. EELS maps (Ti in green and Ni in red) of a p^+n-Si photoanode protected with TiO_2 ALD-deposited at 300 ºC and NiFe decorated a) after fabrication, b) after 100 cycles in 1 M KOH and c) after 400 h stability test in 1 M KOH at 1.3 V vs RHE under 1 sun illumination.

(a)

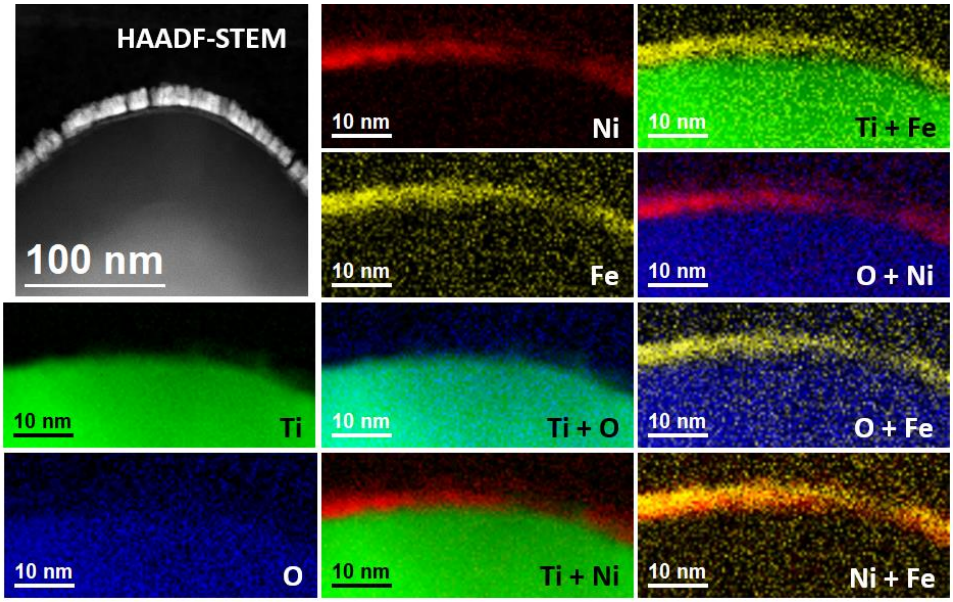

(b)

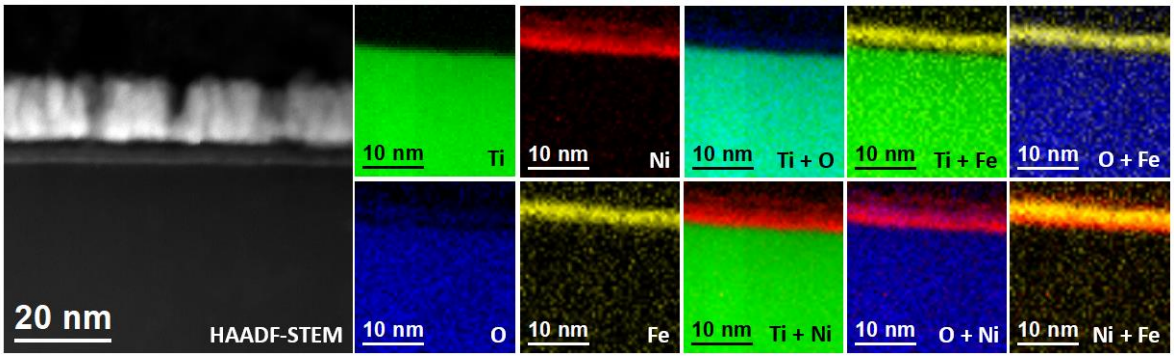

Figure S5: HAADF-STEM image and EELS maps of a p^+n-Si photoanode protected with TiO_2 ALD-deposited at 150 ºC and NiFe decorated before (a) and after electrochemical cycling (b)

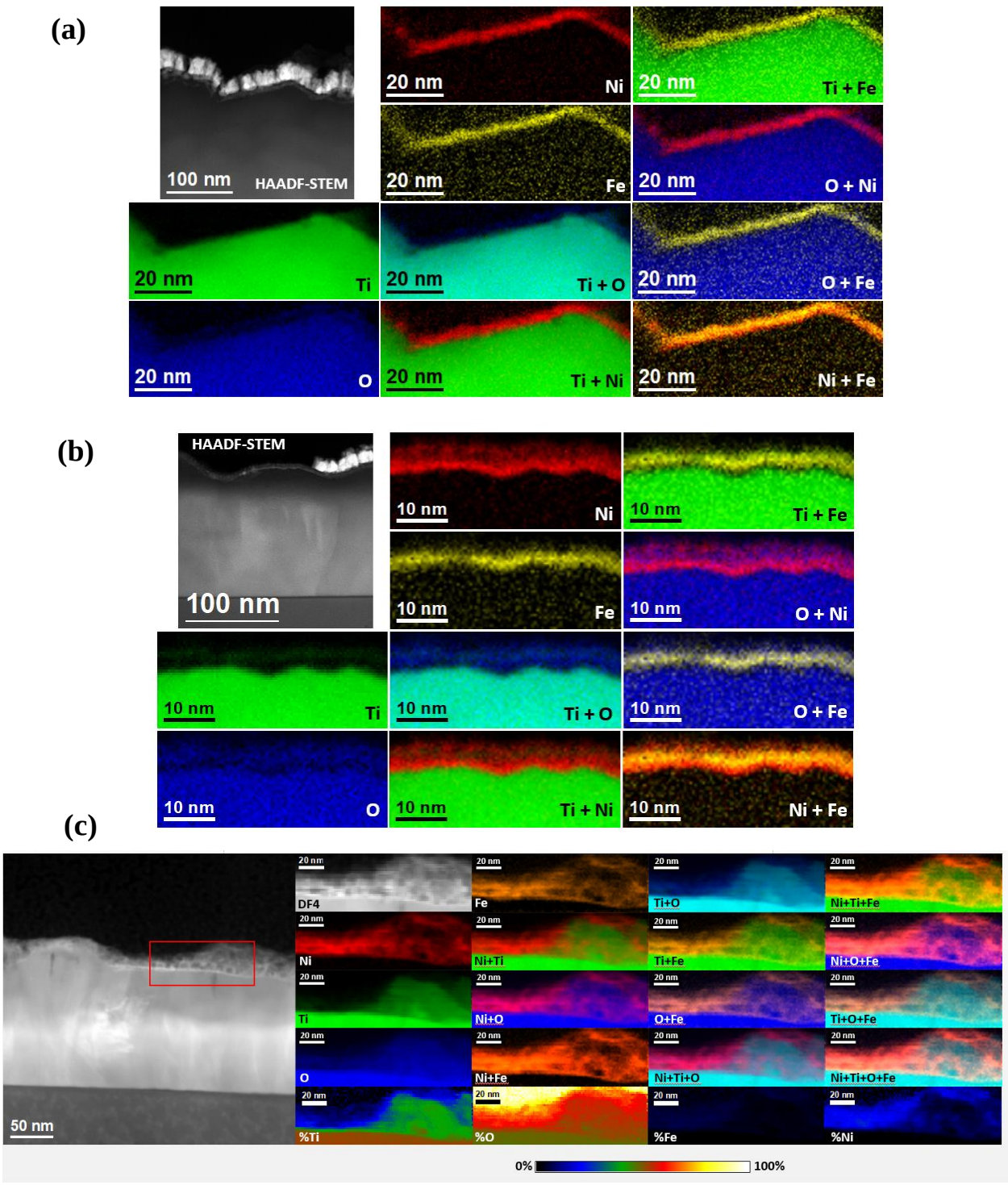

Figure S6: HAADF-STEM image and EELS maps of a $p^{+}n$-Si photoanode protected with TiO_2 ALD-deposited at 300 ºC and NiFe decorated, as synthetized (a), after electrochemical cycling (b), and after stability (c)

XPS analysis.

Table S1: *XPS detection percentage of selected elements for photoanodes with different ALD growth temperature and NiFe decorated, as prepared and after cycling in 1 M KOH.*

	C1s (%)	O1s (%)	Ti2p (%)	Fe2p (%)	Ni2p (%)
150 ºC + NiFe	52.47	34.09	0.19	3.13	10.12
150 ºC + NiFe cycled	39.93	41.5	0.35	4.93	13.29
300 ºC + NiFe	47.75	35.89	0.37	4.67	11.32
300 ºC + NiFe cycled	35.56	45.56	0.47	4.95	13.46

The catalyst presents an average Ni:Fe ratio of 2.8:1. An increase of the oxygen content can be detected after cycling, pointing at oxidation of the catalyst layer by the alkaline electrolyte, OH^- intercalation and the anodic electrochemical potentials applied during cycling, corroborating the previous results obtained by HRTEM and EELS.

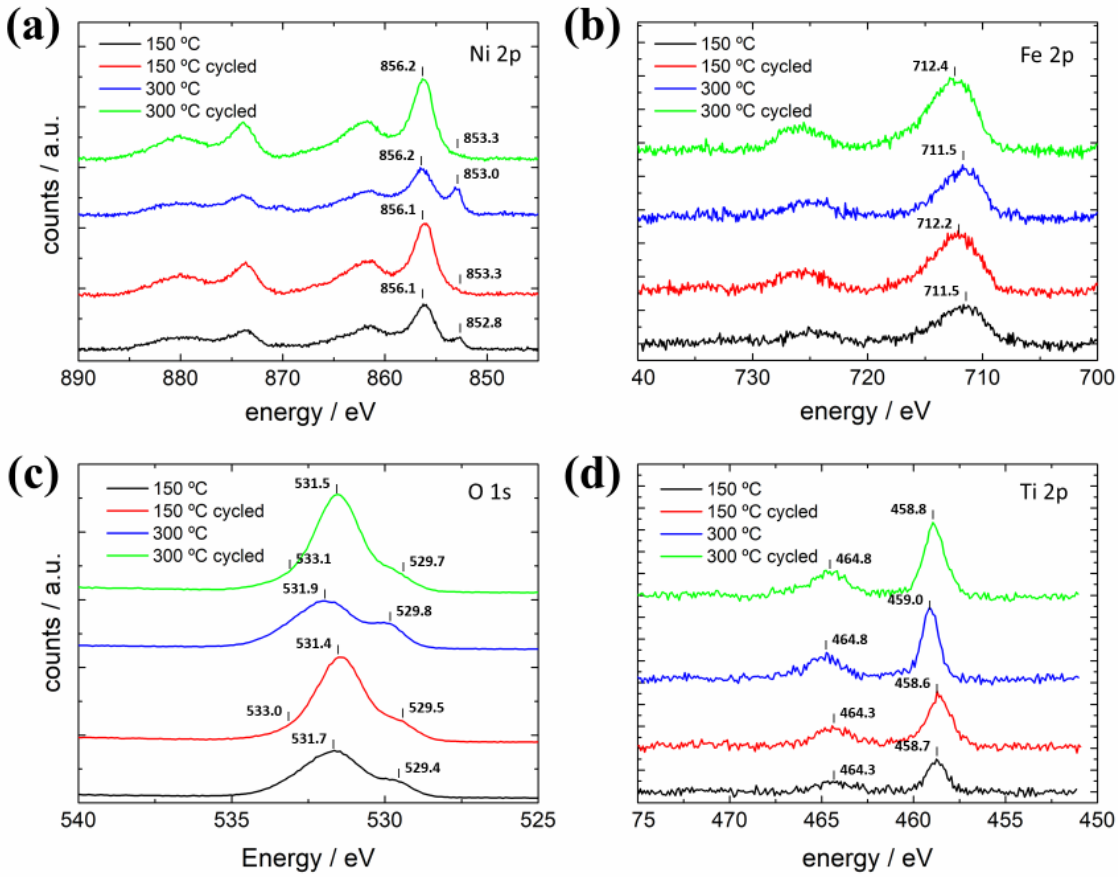

Figure S7. XPS spectra of samples with 150 ºC and 300 ºC deposited TiO_2 layers and NiFe catalyst as prepared and after cycling in 1 M KOH of a) Ni 2p b) Fe 2p c) O 1s and d) Ti 2p peaks.

Analyzing the electronic core-level photoemission peaks more in detail, significant differences are observed for samples with TiO_2 deposition temperatures of 150 and 300 ºC and after cycling them in 1 M KOH (Figure S7).

Analyzing the electronic core-level photoemission peaks more in detail, significant differences are observed for samples with TiO_2 deposition temperatures of 150 and 300 ºC and after cycling them in 1 M KOH (Figure S7).

Analyzing the **Ni2p3/2 peak**, we can observe at bonding energy of ~853 eV the presence of the Ni(0) metallic peak in the samples as prepared, which indicates the incomplete native oxidation caused by atmospheric oxygen[1] and completely disappearing after cycling, which indicates complete oxidation, also corroborated by the increase in the Ni(II) and Ni(III) peaks (~ 856.2 eV). Apart from this, fitting the Ni2p peaks to a specific Ni(II) or Ni(III) chemical state is difficult, as

NiO, $Ni(OH)_2$, and NiOOH share various peak energies[2], but differ on the ratio between these peaks[3]. The high percentage detected for the peak at ~856.2 eV (> 40%) correlated with $Ni(OH)_2$/NiO/NiOOH species, demonstrates that most probably, the catalytic film is composed of all of these chemical states[4,5].

Concerning the **Fe2p3/2 peak**, there is no presence of metallic iron, and the signal can be attributed to Fe (III) species as the binding energy is around 711,5 eV, and for Fe(II) species this value is lower. After cycling, peaks suffer a slight shift towards higher energies (~0.5 eV). The signal-to-noise ratio, although showing Fe(III) peaks, does not allow us to differentiate between $NiFe_2O_4$, FeOOH or Fe_2O_3[6,7]. As Fe is almost 3 times less abundant than Ni in these samples, all of it can be expected to be intercalated forming mostly Ni(Fe)OOH.

O1s signal is mainly attributed either to Ni or Fe coordination. Two clear peaks can be seen for uncycled samples, one corresponding to metal oxides (~529.5 eV) and another one which could be ascribed to metal hydroxides (~531.5 eV)[3]. In the cycled samples, a third peak is detected at 533.1 eV, which is attributed to physisorbed water (533.5 eV)[3]. Also, the hydroxide peak becomes much more predominant over the oxides, as it should be expected[1,6], together with absolute higher oxygen content detected, caused by the oxidation of the metallic Ni-Fe and the corresponding OH intercalation.

Regarding the **Ti2p peaks** of all samples, the main peak at ~458.7 eV can be attributed to the Ti (IV) 2p3/2 with the corresponding 2p1/2 peak at 464.3 eV[8].

Valence Band Studies. After 5 nm NiFe coating is thermally evaporated on top of TiO_2 grown at 150 and 300 ºC, metallic behaviour is detected. NiFe layer before cycling has mainly a metallic nature with a partial contribution of a native oxide, which predominantly oxidized afterwards but still with free electrons, being former ones the responsible of signal at lower than 0 eV. Two slopes can be assigned for cycled samples (Fig.S8 cyan and pink), one to p-type semiconductor and another one to free electrons at energies slightly lower than 0 eV. The active catalyst, named as nanostructured Ni(Fe)OOH presents electronic structures significantly different from bulk NiO due to significant interaction with the alkaline electrolyte, surface states, three dimensional flakes nanostructure, and porosity[9]. The slightly higher Fermi level for 300 ºC sample is translated to

lower energies for all cases, as all Fermi levels must equilibrate. Samples with NiFe have around ~3 eV lower energy than bare TiO_2 ones. This matches TiO_2 valence band plus TiO_2 band gap, meaning there is a good band alignment between TiO_2 conduction band and the NiFe catalyst.

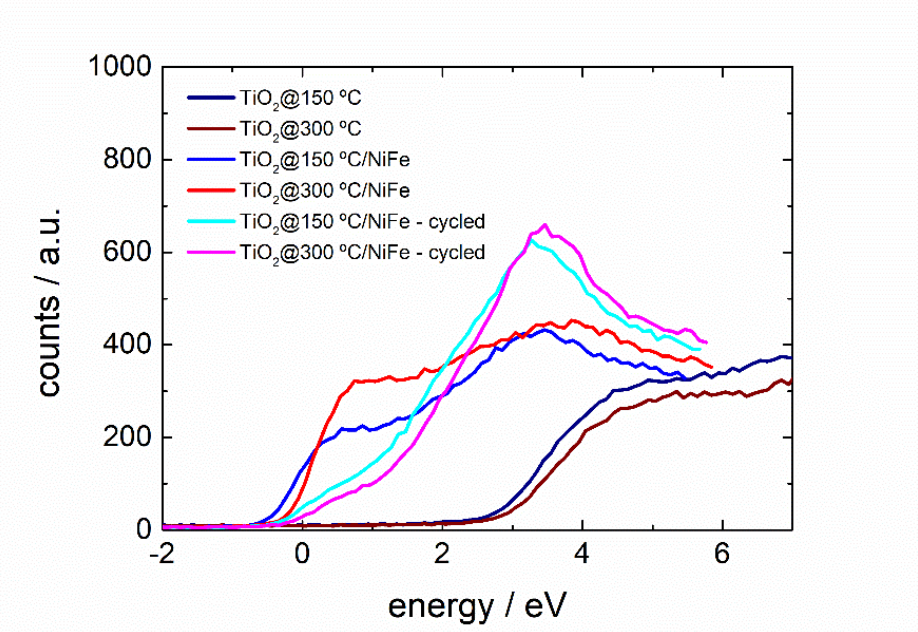

Figure S8. XPS spectra of samples with TiO_2 protective layers ALD grown at 150 and 300 ºC, without NiFe catalyst, with it, and with the catalyst after cycling to oxidative potentials in 1 M KOH under 1 sun illumination.

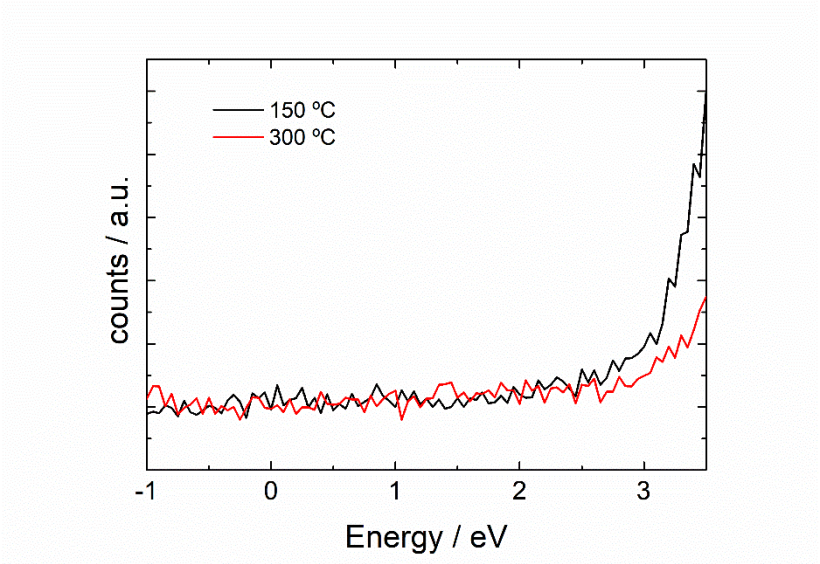

Figure S9. Fine XPS analysis of the 0-3 eV region presenting no visible intra-band gap states such as other works have shown[10] for samples grown at 150 and 300 ºC.

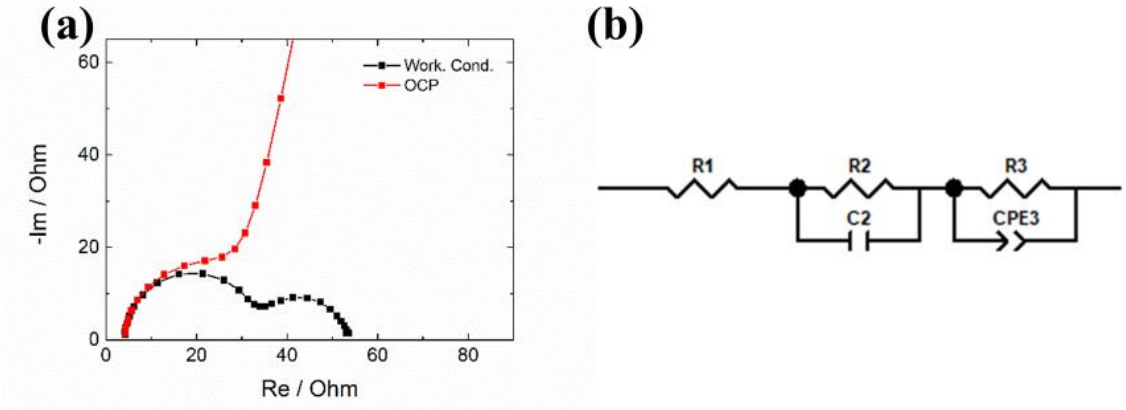

Figure S10. a) EIS measurements of a p^+-Si anode TiO_2 protected at 300 ºC and NiFe decorated set to 1.8 V vs RHE (Working Conditions) and to open circuit potential (OCP) in dark and in 1 M KOH as electrolyte. The first semicircle is independent of applied potential and the second one varies significantly, proving a non-Ohmic dependence of this second one. b) scheme of the electrical circuit used to fit measured impedance data.

Table S2. *Fitted values of Figure S10*

	R_1 (Ω)	R_2 (Ω)	C_2 (F· cm^{-2})	R_3 (Ω)	CPE_3 (F· cm^{-2} ·$s^{\alpha 3-1}$)	α_3
1.8 V VS RHE	4.148	27.8	1.59E-06	21.79	2.67E-04	0.85
OCP	4.108	23.51	1.50E-06	3.15E+05	2.99E-05	0.87316

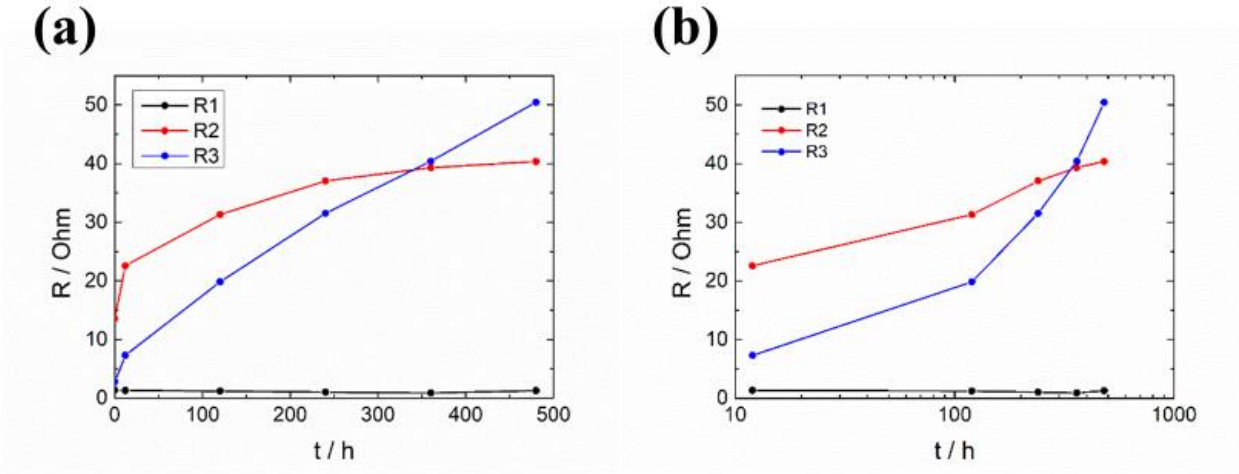

Figure S11. Variation of resistances over time in linear scale (a) and linear-log scale (b) for a p^+-Si anode protected with TiO_2 ALD-deposited at 300 ºC and NiFe decorated in 1 M KOH at a fixed potential of 1.8 V vs RHE.

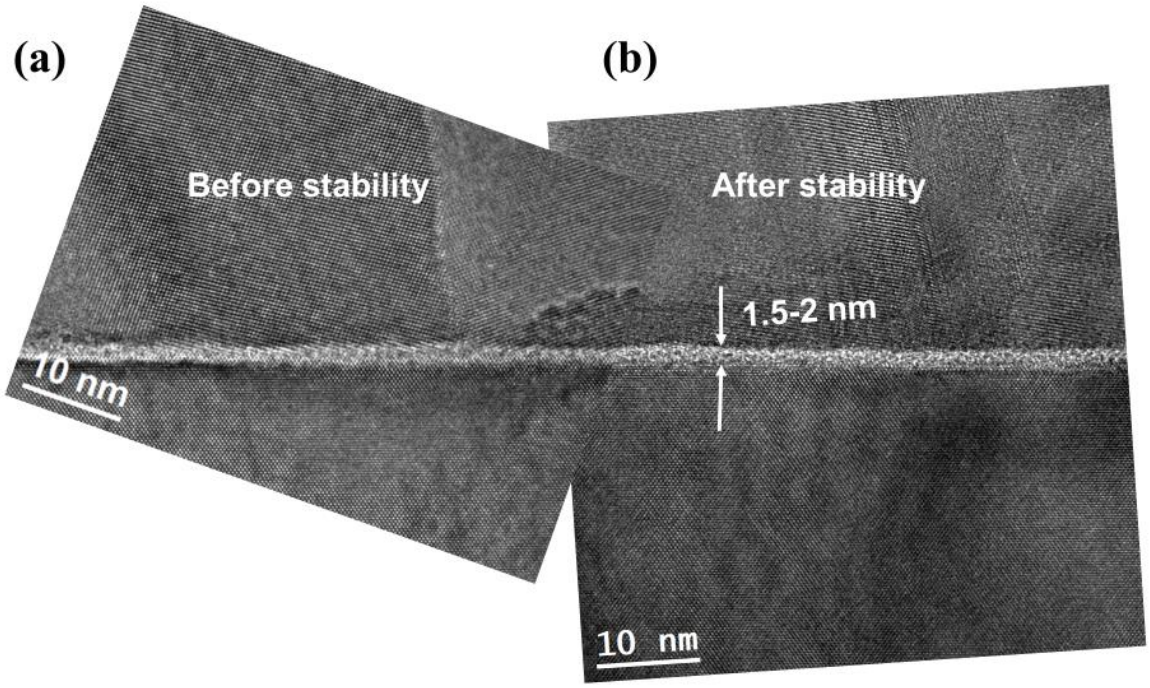

Figure S12. HTREM analysis of the SiO_x layer a) before and b) after the stability measurement of a photoanode after 400 hours of stability at 1.8 V vs RHE. No significant growth can be observed. Increase of the SiO_2 interlayer could be a reason to dramatically increase tunnelling resistivity[11], as reported in other works[12].

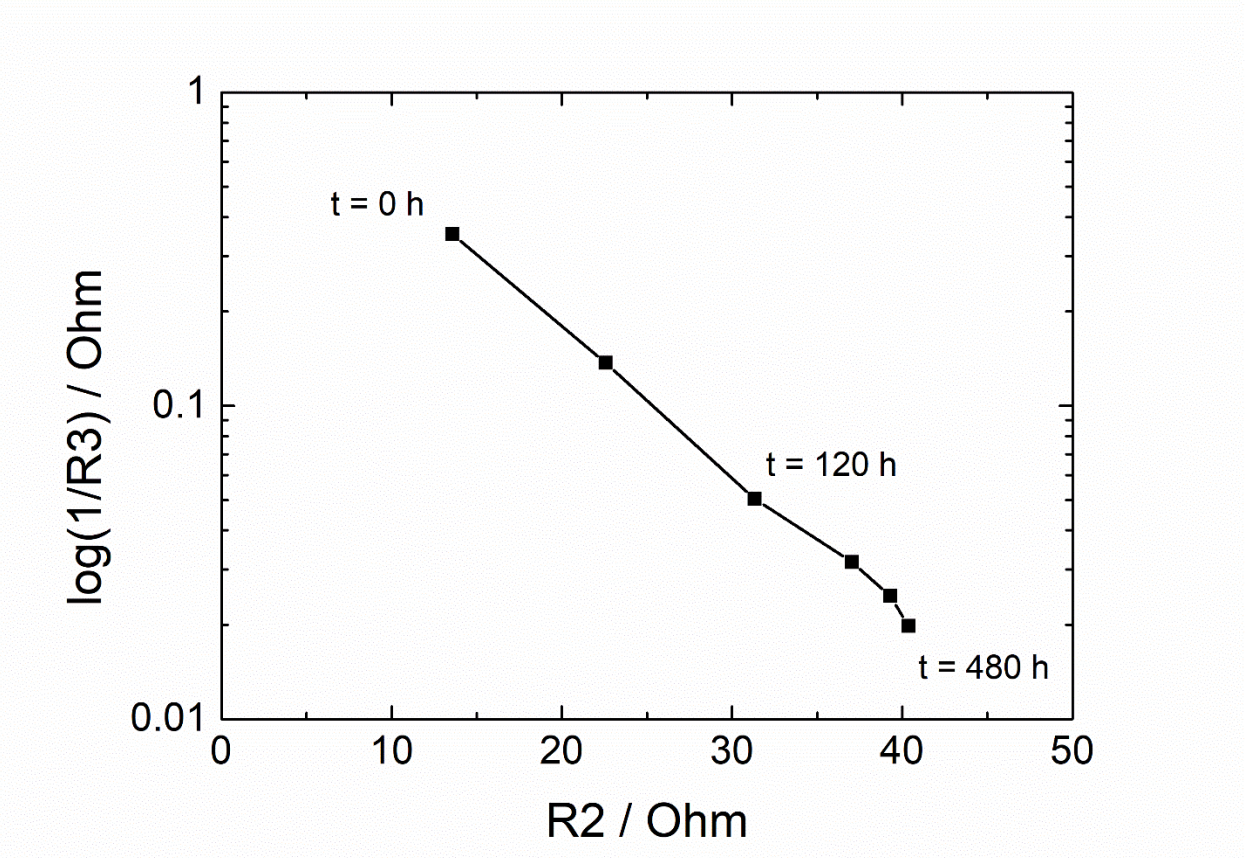

Figure S13. Representation of fitted values in Table1, log(1/R3) as a function of R2.

Table S3. EIS fittings in open circuit potential (OCP) conditions corresponding to Fig. 7b measured data.

#measure	R_1 (Ohm·cm^2)	R_2 (Ohm·cm^2)	C_2 (F· cm^{-2})	R_3 (Ohm·cm^2)	CPE_3 (F· cm^{-2} ·S^{A3-1})	A_3
1	5.49	4753.0	$1.95 \cdot 10^{-6}$	3581.0	$1.85 \cdot 10^{-5}$	0.817
2	4.50	167.2	$1.79 \cdot 10^{-6}$	118.3	$3.97 \cdot 10^{-4}$	0.561
3	4.49	145.2	$1.77 \cdot 10^{-6}$	113.4	$5.44 \cdot 10^{-4}$	0.530
4	5.27	3686.0	$1.76 \cdot 10^{-6}$	1948.0	$4.79 \cdot 10^{-5}$	0.742

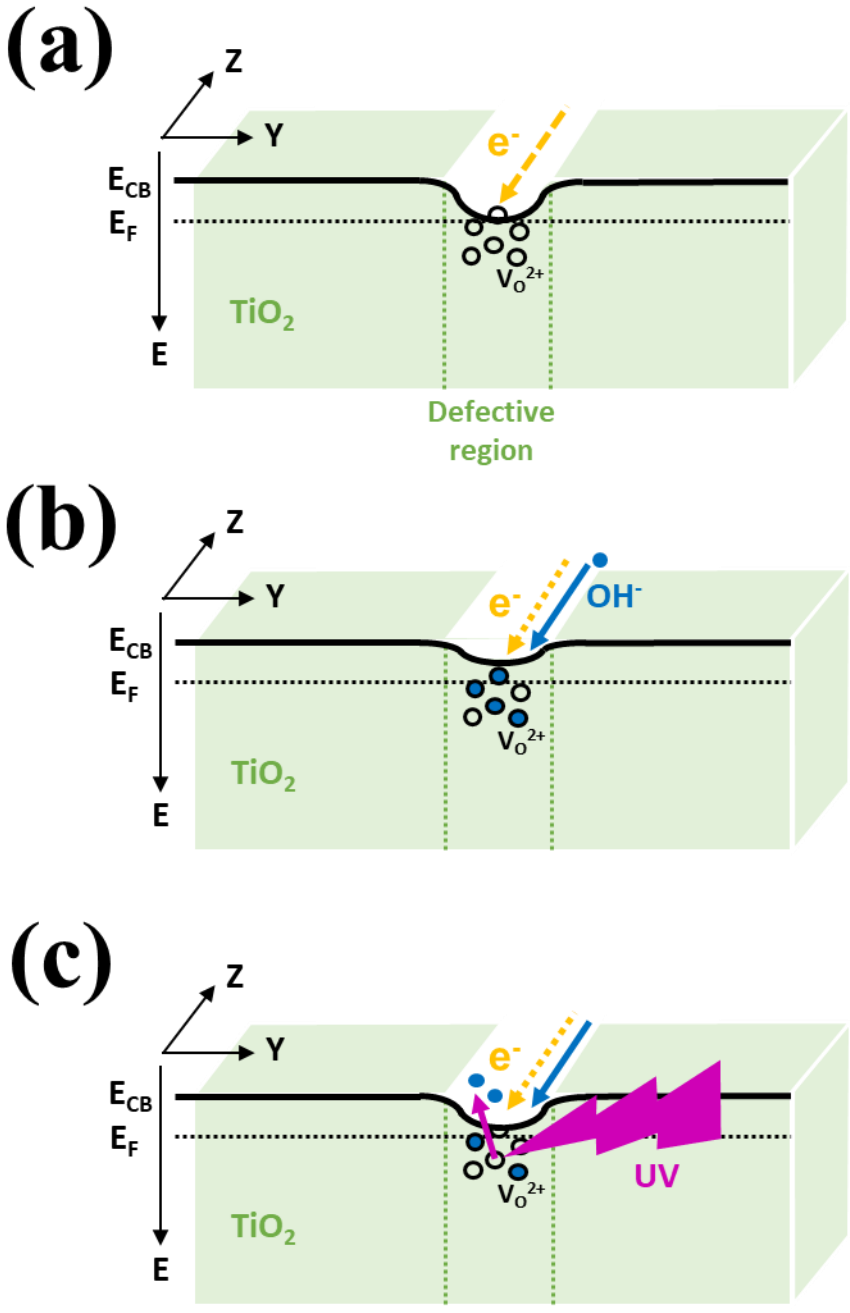

Scheme S1: energy and cross section diagram corresponding to a preferential path region, showing a) extra states in interfacial defects generate a preferential path, b) OH^- diffusion and oxygen vacancy occupation and c) UV excitation of these states, partially recovering the initial oxygen vacancy abundance.

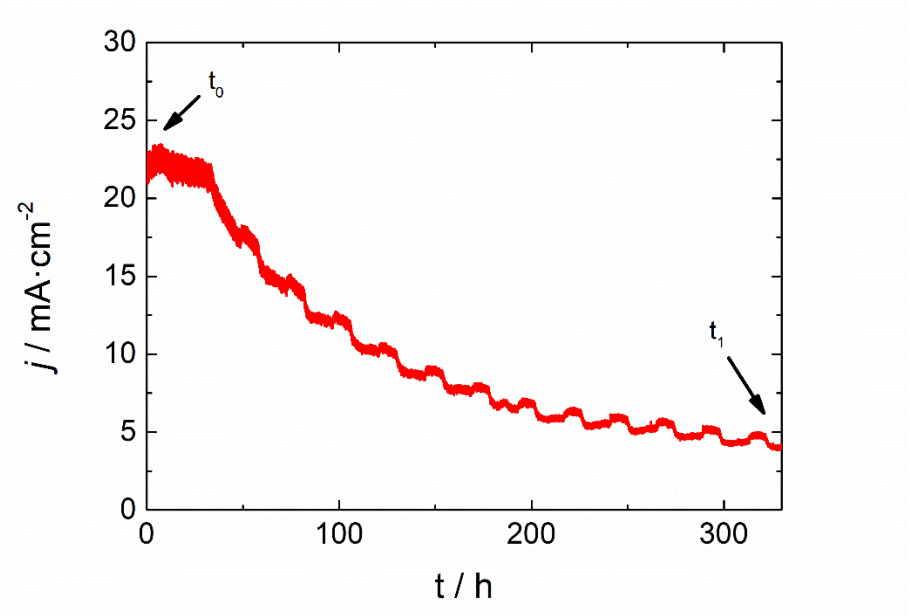

Figure S14. Current stability measurement of a p^+n-Si photoanode protected with TiO_2 ALD-deposited at 300 ºC and NiFe decorated at a fixed potential of 1.3 V vs RHE (Observed ondulations every 24h are caused by lab temperature variations at night and day). Measurements performed under 1 sun illumination, using 1 M KOH as electrolyte.

References

(1) Han, T.; Shi, Y.; Song, X.; Mio, A.; Valenti, L.; Hui, F.; Privitera, S.; Lombardo, S.; Lanza, M. Ageing Mechanisms of Highly Active and Stable Nickel-Coated Silicon Photoanodes for Water Splitting. *J. Mater. Chem. A* **2016**, *4* (21), 8053–8060.

(2) Biesinger, M. C.; Lau, L. W. M.; Gerson, A. R.; Smart, R. S. C. The Role of the Auger Parameter in XPS Studies of Nickel Metal, Halides and Oxides. *Phys. Chem. Chem. Phys.* **2012**, *14* (7), 2434–2442.

(3) Biesinger, M. C.; Payne, B. P.; Grosvenor, A. P.; Lau, L. W. M.; Gerson, A. R.; Smart, R. S. C. Resolving Surface Chemical States in XPS Analysis of First Row Transition Metals, Oxides and Hydroxides: Cr, Mn, Fe, Co and Ni. *Appl. Surf. Sci.* **2011**, *257* (7), 2717–2730.

(4) Digdaya, I. A.; Adhyaksa, G. W. P.; Trzesniewski, B. J.; Garnett, E. C.; Smith, W. A. Interfacial Engineering of Metal-Insulator-Semiconductor Junctions for Efficient and Stable Photoelectrochemical Water Oxidation. *Nat. Commun.* **2017**, *8* (May), 15968.

(5) Mei, B.; Permyakova, A. a; Frydendal, R.; Bae, D.; Pedersen, T.; Malacrida, P.; Hansen, O.; Stephens, I. E. L.; Vesborg, P. C. K.; Seger, B.; et al. Iron-Treated NiO as a Highly Transparent p - Type Protection Layer for E Ffi Cient Si-Based Photoanodes. *J. Phys. Chem. Lett.* **2014**, *5* (20), 3456–3461.

(6) Zhou, H.; Yu, F.; Zhu, Q.; Sun, J.; Qin, F.; Yu, L.; Bao, J.; Yu, Y. Water Splitting by Electrolysis at High Current Density under 1.6 Volt. *Energy Environ. Sci.* **2018**, No. 60 mL, 3–5.

(7) Lu, Z.; Xu, W.; Zhu, W.; Yang, Q.; Lei, X.; Liu, J.; Li, Y.; Sun, X.; Duan, X. Three-Dimensional NiFe Layered Double Hydroxide Film for High-Efficiency Oxygen Evolution Reaction. *Chem. Commun.* **2014**, *50* (49), 6479–6482.

(8) Biesinger, M. C.; Lau, L. W. M.; Gerson, A. R.; Smart, R. S. C. Resolving Surface Chemical States in XPS Analysis of First Row Transition Metals, Oxides and Hydroxides: Sc, Ti, V, Cu and Zn. *Appl. Surf. Sci.* **2010**, *257* (3), 887–898.

(9) Dette, C.; Hurst, M. R.; Deng, J.; Nellist, M. R.; Boettcher, S. W. Structural Evolution of Metal (Oxy)Hydroxide Nanosheets during the Oxygen Evolution Reaction. **2018**.

(10) Hu, S.; Shaner, M. R.; Beardslee, J. a; Lichterman, M.; Brunschwig, B. S.; Lewis, N. S. Amorphous TiO_2 Coatings Stabilize Si, GaAs, and GaP Photoanodes for Efficient Water Oxidation. *Science* **2014**, *344* (6187), 1005–1009.

(11) Scheuermann, A. G.; Kemp, K. W.; Tang, K.; Lu, D. Q.; Satterthwaite, P. F.; Ito, T.; Chidsey, C. E. D. D.; McIntyre, P. C.; Mc Intyre, P. C. Conductance and Capacitance of Bilayer Protective Oxides for Silicon Water Splitting Anodes. *Energy Environ. Sci.* **2016**, *9* (2), 1–26.

(12) Kiseok Oh, a Cristelle Meriadec, b Benedikt Lassalle-Kaiser, c Vincent Dorcet, a Bruno Fabre, A.; Soraya Ababou-Girard, b Loic Joanny, d F. G. and G. L.; Oh, K.; Meriadec, C.; Lassalle-Kaiser, B.; Dorcet, V.; Fabre, B.; Ababou-Girard, S.; Joanny, L.; Gouttefangeas, F.; et al. Elucidating the Performance and Unexpected Stability of Partially Coated Water-Splitting Silicon Photoanodes. *Energy Environ. Sci.* **2018**, 0–11.